Tuned vibration modes in a miniature hearing organ: Insights from the bushcricket

Anna Vavakou[a], Jan Scherberich[b], Manuela Nowotny[b], and Marcel van der Heijden[a,1]

[a]Department of Neuroscience, Erasmus MC, University Medical Center Rotterdam, 3000 CA, Rotterdam, The Netherlands; and [b]Institute for Zoology and Evolutionary Research, Friedrich Schiller University Jena, 07743 Jena, Germany

Edited by Daniel Robert, University of Bristol, Bristol, United Kingdom, and accepted by Editorial Board Member Thomas D. Albright August 17, 2021 (received for review March 17, 2021)

Bushcrickets (katydids) rely on only 20 to 120 sensory units located in their forelegs to sense sound. Situated in tiny hearing organs less than 1 mm long (40× shorter than the human cochlea), they cover a wide frequency range from 1 kHz up to ultrasounds, in tonotopic order. The underlying mechanisms of this miniaturized frequency-place map are unknown. Sensory dendrites in the hearing organ (crista acustica [CA]) are hypothesized to stretch, thereby driving mechanostransduction and frequency tuning. However, this has not been experimentally confirmed. Using optical coherence tomography (OCT) vibrometry, we measured the relative motion of structures within and adjacent to the CA of the bushcricket *Mecopoda elongata*. We found different modes of nanovibration in the CA that have not been previously described. The two tympana and the adjacent septum of the foreleg that enclose the CA were recorded simultaneously, revealing an antiphasic lever motion strikingly reminiscent of vertebrate middle ears. Over the entire length of the CA, we were able to separate and compare vibrations of the top (cap cells) and base (dorsal wall) of the sensory tissue. The tuning of these two structures, only 15 to 60 μm (micrometer) apart, differed systematically in sharpness and best frequency, revealing a tuned periodic deformation of the CA. The relative motion of the two structures, a potential drive of transduction, demonstrated sharper tuning than either of them. The micromechanical complexity indicates that the bushcricket ear invokes multiple degrees of freedom to achieve frequency separation with a limited number of sensory cells.

insect hearing | optical coherence tomography | crista acustica | *Mecopoda elongata*

A hearing organ converts sound-induced mechanical vibrations to receptor potentials that are further processed along the auditory pathway. Bushcrickets (katydids) *Mecopoda elongata* (Insecta, Orthoptera, Tettigoniidae) have a miniature hearing organ, the crista acustica (CA), that is located in their front tibia and can sense frequencies up to 70 kHz (1). To achieve that, they rely on less than 50 sensory units (2, 3), each consisting of a sensory cell, a cap cell (CC), and a scolopale cell (Fig. 1*D*; see Fig. 3*B*). The total length of the CA is ∼0.9 mm, which is ∼40 times shorter than the uncoiled cochlea in humans. Still, the CA with its limited cellular machinery is able to mechanically separate a wide range of frequencies, but the underlying mechanisms are not well understood.

In bushcrickets, the sound-induced nanovibrations reach the sensory tissue through two routes. The main source of airborne sound is the spiracle (4), a horn-shaped opening in the thorax that delivers and enhances the sound input to the CA via an acoustic trachea (5–7). Second, the two tympana on the anterior and posterior sides of the front legs are also reported to deliver sound to the sensory tissue (8, 9). The sensory units of the CA are surrounded by haemolymph fluid and are protruding from the dorsal side of the dorsal wall (DW) of the acoustic trachea. Each ciliated tip of a sensory dendrite is embedded in the cap of a CC (Fig. 1*D*; see Fig. 3*B*). These CCs are part of a continuous tectorial membrane that connects the sensory units (10). Transduction takes place as the mechanosensitive channels on the sensory dendrite open due to displacement of the CC (11, 12). The CA in bushcricket ears is tonotopically organized along the proximal–distal axis (12–14) following an anatomical gradient, with increasing height and width of the sensory units (3, 15) toward the proximal end. Mechanical measurements of sound-induced responses revealed that high frequencies induce greater motion magnitude in the distal part of the CA (16, 17). Spatial phase gradients in tone-evoked vibrations indicate the existence of waves traveling from the distal, high-frequency end to the proximal end of the CA (16). Whereas traveling waves in the mammalian cochlea accumulate several cycles of phase delay (18), the total phase accumulation in the bushcricket CA is only 0.5 to 1 cycle (19). The exact mechanisms that drive transduction and tonotopy in the CA are undefined.

Recently, it was reported that the mechanical responses of the CA show different frequency tuning than the neural response at the same location (12). The CCs are located dorsally to the DW, and the dendrite of the sensory neuron is approximately perpendicular to the DW. The relative motion between the two structures may drive the opening of the transduction channels and could explain discrepancies between mechanical and neural tuning. However, it has not been possible to probe such relative motion experimentally due to technical limitations of the technique used in laser Doppler vibrometry (LDV), which has

Significance

Most hearing organs contain an array of sensory cells that act as miniature microphones, each tuned to its own frequency like piano strings. Acoustically communicating insects like bushcrickets have evolved miniscule hearing organs, typically smaller than 1 mm, in their forelegs. It is still unknown how the sensory structures inside the leg vibrate in response to sound. Using advanced imaging techniques, we meticulously mapped the nanovibrations in the bushcricket ear. We discovered a complex motion pattern in which structures separated by only 1/50 mm showed systematic tuning differences. Despite the insect ear's tiny dimensions, its mode of operation strikingly resembled that of vertebrate ears. Apparently, evolution has provided similar solutions to the spectral processing of sounds.

Author contributions: A.V., J.S., M.N., and M.v.d.H. designed research; A.V., J.S., M.N., and M.v.d.H. performed research; A.V. and M.v.d.H. analyzed data; and A.V., J.S., M.N., and M.v.d.H. wrote the paper.

The authors declare no competing interest.

This article is a PNAS Direct Submission. D.R. is a guest editor invited by the Editorial Board.

See online for related content such as Commentaries.

[1]To whom correspondence may be addressed. Email: marcel.vdh.work@gmail.com.

This article contains supporting information online at https://www.pnas.org/lookup/suppl/doi:10.1073/pnas.2105234118/-/DCSupplemental.

Published September 22, 2021.

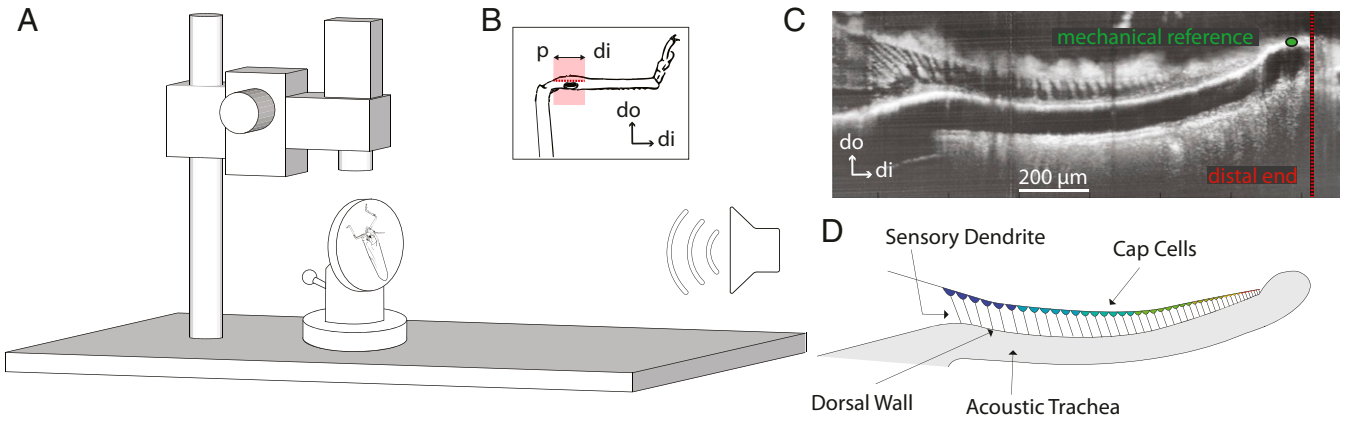

Fig. 1. OCT imaging. (*A*) Illustration of the experimental setup. The fixed animal was placed under the OCT vibrometer, and sound was delivered using an open-field stimulation paradigm. (*B*) Schematic drawing of the foreleg that holds the hearing organ, CA, including a proximal–distal/dorsal–ventral section of the CA. (*C*) A cross-section OCT image ("B scan") obtained from the top view of the hearing organ, following an image section plane as shown in *B*, across the proximal–distal axis. (*D*) Sketch relating the B scan to the anatomy across the proximal–distal axis. The DW and the CCs can be identified. The CA position at the distal end indicated with the green circle is the reference position used in this study to normalize sound-induced vibrations. By convention, all the distances are expressed relative to the red line that illustrates the very distal part of the CA. di, distal; do, dorsal; p, proximal.

been extensively used to measure vibrations in insect hearing organs (16).

LDV measurements do not provide inherent depth resolution, and the optical inhomogeneities of biological tissues cause diffraction, scattering, and lensing effects that adversely affect optical focus. Therefore, most LDV measurements in the insect hearing organs were done on the most accessible and reflective structures, like the tympana (20), antenna (21), and cuticle, as an indirect measurement of organ motion (17). Measurements of hearing organ motion were also obtained through a transparent cuticle (22) or after the surgical removal of the cuticle (16). Optical coherence tomography (OCT) provides opportunities to reliably attribute vibrations to anatomical structures, as it resolves depth and allows for fast nanovibrometry measurements (23). OCT has yielded vibration maps of cross-sections of the mammalian organ of Corti (24) and the description of different vibration modes of the cochlear partition (25). The new OCT results revealed structural interconnections in the micromechanics that stirred up the understanding of cochlear function (26) but have not yet been used to shed light on the operation of insect hearing organs.

In the current study, we used OCT vibrometry to perform noninvasive measurements of nanovibrations in the bushcricket hearing organ. First, we used this technique to describe the relative motion of the two tympana and the septum of the trachea (Fig. 2) in response to broadband, multitone sound stimuli. Next, we approached the CA from the dorsal side (Fig. 1*B*) to perform simultaneous vibration measurements of the CC and the DW, and this allowed us to determine the relative motion between these closely neighboring structures. We observed systematic differences in the frequency-place map and sharpness between CC and DW. The relative motion between CC and DW was found to be more sharply tuned than either of the individual structures.

Results

The Relative Motion of the Two Tympana. The two tympana are easily accessible for imaging in a noninvasive manner, so they were the first structures we aimed to study. For this purpose, the OCT recording beam was aimed perpendicular to the anterior tympanum. When imaging through the anterior tympanum, the recording beam traverses through the tracheal septum before it reaches the posterior tympanum. Light intensity can be a limiting factor when imaging with the OCT as highly reflective surfaces tend to obscure deeper structures. Our results demonstrate that with our setup, it is possible to image both tympana and identify them with certainty (Fig. 2 *A* and *D*), which afforded a means to record sound-induced vibrations on the two tympana (Fig. 2 *B* and *C*) simultaneously. By doing so, we exclude any effects that rotating the preparation has on the acoustic delivery of the stimulus.

The color map in Fig. 2*B* illustrates how the phase of the vibrations is distributed along the B scan (details are in *Response Analysis*) for a 14.3-kHz stimulus at 79 dB sound pressure level (SPL). The motion of each tympanum had a constant phase profile along the recorded width, from the dorsal end until halfway to the ventral end. The two tympana moved with an ∼0.5-cycle (=180°) phase difference, and this phase opposition was consistent across the whole recorded width of the tympana. Across different frequencies (0.4 to 38 kHz), the two tympana shared similar vibration magnitudes (Fig. 2*F*) and showed an ∼0.5-cycle phase difference (Fig. 2 *B* and *E*), confirming previous findings (27). For both tympana, the magnitude followed a dorsal–ventral displacement gradient, with the higher values toward the ventral side (Fig. 2*C*). Both tympana describe a hinged motion anchored at their dorsal ends (Fig. 2*G*). These observations were systematic across all our tympanum measurements (n = 11 bushcricket legs) (*SI Appendix*, Fig. S1).

In addition to the two tympana, we were also able to observe the phase of the vibrations on the anterior part of the DW and the tracheal septum, a structure splitting the acoustic trachea in two compartments, for which no vibration data have been reported before (Fig. 2*B*). In Fig. 2*B*, the anterior end of the CA is seen to move in phase with the anterior tympanum (deepest cyan squares), while the septum moves in phase with the posterior tympanum (dark orange squares halfway between the two tympana). These structures are very close to the sensory unit, and their antiphasic motion could be of functional significance if it resulted in a mechanical stress on the CA that could be felt by the sensory dendrites. We did, however, not further pursue this analysis here because the anterior–posterior viewing angle is suboptimal for studying relative motions within the sensory unit; the DW in particular is hardly visible. Instead, we studied the DW motion along the dorsal–ventral axis, where it is clearly visible.

Micromechanics: Dissecting the Motion within the CA. Aiming to explore further motions within the sensory units, we imaged the CA through a dorsal view as illustrated in Figs. 1 and 3. That

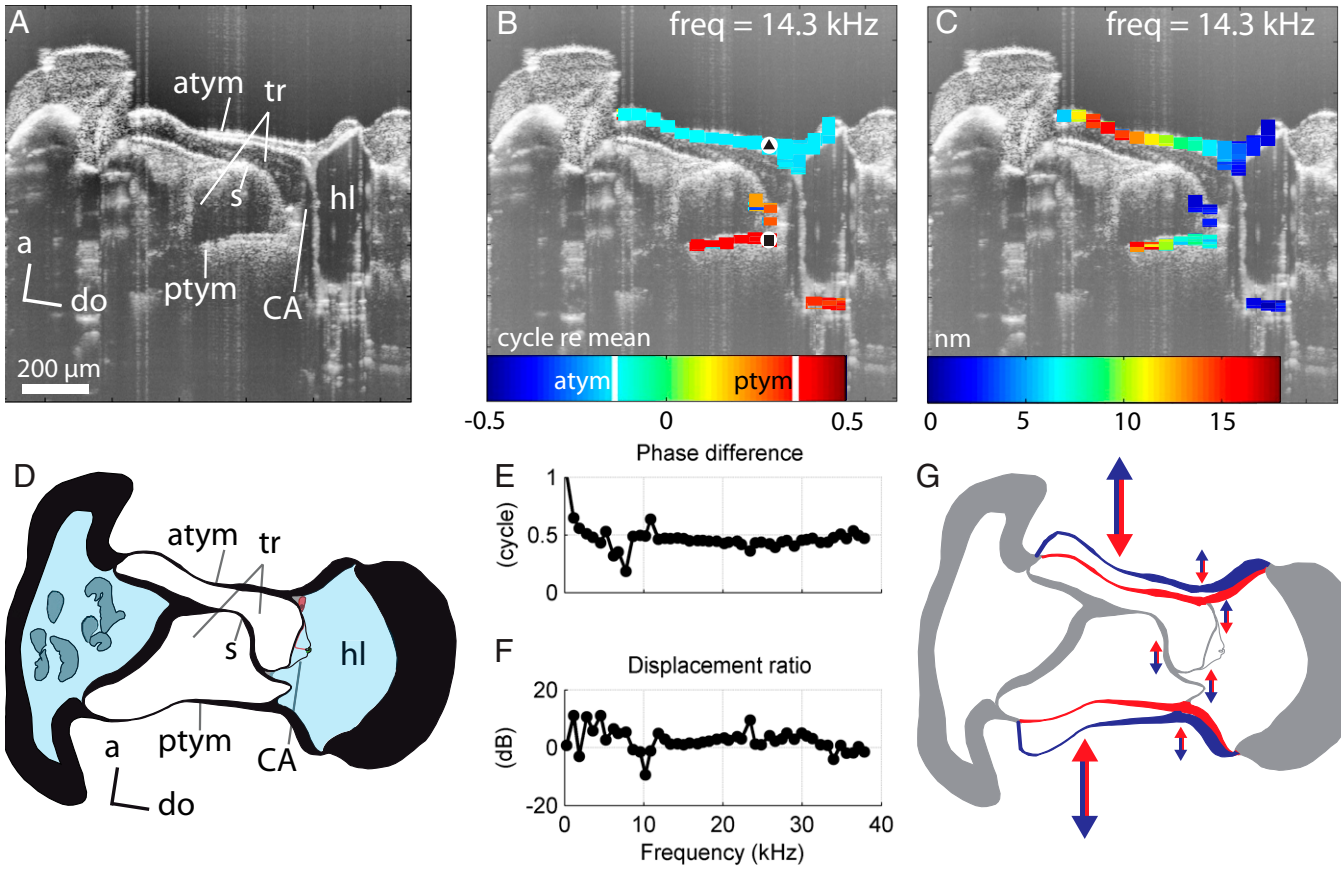

Fig. 2. Mechanical responses of the anterior and posterior tympana to sound stimulation. (*A*) OCT B scan of a front leg viewed through the anterior tympanum. (*B*) The same B scan overlaid with color-coded phase information for a stimulus frequency of 14.3 kHz presented at 79 dB SPL. Notice that a phase difference of 0.5 cycles is 180° (an out-of-phase motion). The hemolymph fluid behind the anterior tympanum caused the position of the dorsal part of the posterior tympanum to shift to a more posterior position. This optical distortion does not affect the vibration data. The white stripes in the color map mark the average phases of the two tympana. (*C*) The same B scan overlaid with the companion color-coded vibration magnitude information. (*D*) Anatomical sketch of a cross-section of the bushcricket front leg. Adapted from ref. 3. (*E*) The displacement phase difference between posterior and anterior tympana across different stimulus frequencies. The mechanical measurements were obtained at the positions indicated by the markers in *B*. (*F*) Displacement magnitude differences between posterior and anterior tympanum across different stimulus frequencies at the marked positions in *B*. (*G*) Two extreme configurations of the tympana within one cycle of stimulus frequency are illustrated with red and blue. Displacement amplitude is enlarged 5,000× for illustration purposes. The two tympana bulge in (red) and out (blue) synchronously. The septum follows the posterior tympanum motion direction. The arrows illustrate the magnitude of vibrations, which increases toward the ventral side of the tympanum. The ventral part of the tympanum moves ∼3.6 times more than close to the CA at the stimulus frequency. The tympana motion resembles a hinge, anchored at the dorsal end. More data are in *SI Appendix*, Fig. S1. a, anterior; do, dorsal; atym, anterior tympanum; hl, hemolymph; ptym, posterior tympanum; s, septum; tr, trachea.

way, our recording beam travels through the CA aligned with the dorsal–ventral anatomical axis, allowing us to distinguish these structures in our B scans. As a consequence, motion of the CC and the DW can be disentangled. The mechanical measurements were normalized to vibrations recorded in the distal end of the CA. The results presented in detail below come from a preparation where vibrations on the CA were measured through the intact dorsal cuticle (BC0007) (details are in *Materials and Methods*).

Using OCT vibrometry, we can expand the datasets in the existing literature. Previous studies have reported a tonotopic response of the CA with high and low frequencies exciting the distal and proximal parts of the organ, respectively (13, 16, 17). The tonotopic gradient coincides with a gradient in the size of the anatomical structures (3). In Fig. 3, the recordings of the DW (black curves) are shown alongside those of the CC (blue curves). Spatial and spectral patterns of the sound-induced CA motion demonstrate the tonotopy in two complementary ways. Fig. 3 *D–F* shows the CA vibration magnitude evoked by three different frequency components (6.3, 12.5, and 23.4 kHz) as a function of longitudinal position, as measured on the DW and the CC. Each of these excitation patterns is peaked; with decreasing frequency, the peak location shifts toward the proximal end. The corresponding phase data (Fig. 3 *G–I*) display an accumulation of ∼0.5 to 1 cycle of phase from the distal end to the peak region. These phase data yielded estimates of wavelength and phase velocity in the peak region as detailed in Fig. 3. Wavelength ranged from 345 to 599 µm (DW) and from 222 to 370 µm (CC); phase velocity ranged from 3.7 to 8.1 m/s (DW) and from 2.4 to 5.2 m/s (CC). These values are consistent with previous reports in *M. elongata* (16, 19).

The spectral representation of tuning is illustrated in Fig. 3 *J–O* by plotting magnitude (Fig. 3 *J–L*) and phase (Fig. 3 *M–O*) as a function of frequency recorded at three positions along the tonotopic axis. The tonotopy and phase patterns in Fig. 3 are consistent with previous reports of CA vibrations (12, 19). The overall tuning and tonotopy of the DW are similar to those of the CC, but we also found systematic differences between the tuning of the two structures in the 5- to 25-kHz frequency range. The differences in tuning between DW and CC will be detailed below.

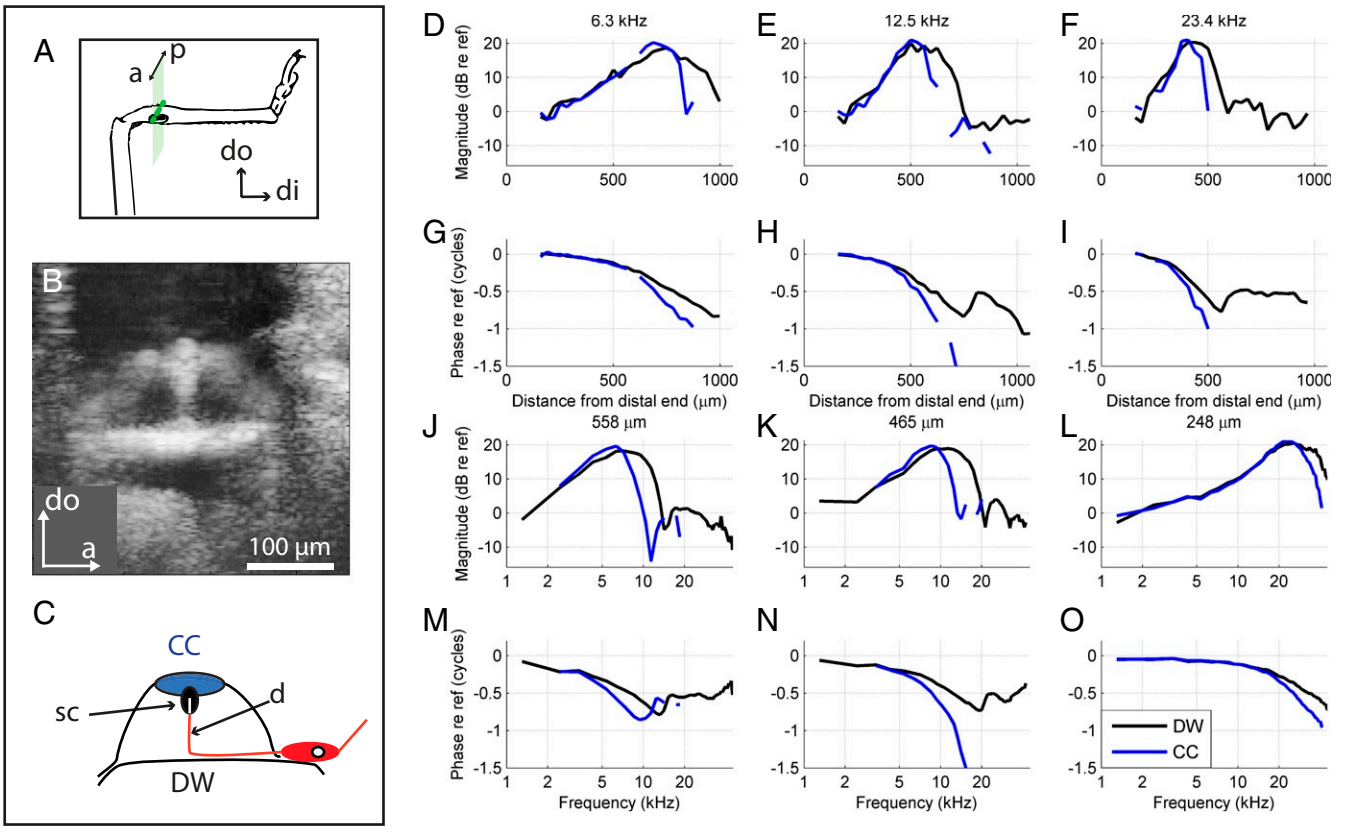

Fig. 3. Differences in the tonotopic response and frequency tuning of the DW and the CCs. (*A*) An anterior–posterior cross-section of the front leg. (*B*) OCT B scan obtained from the top view of the CA, following an image section plane as shown in *A*, across the anterior–posterior axis. (*C*) Sketch relating the B scan to the anatomy across the anterior–posterior axis. The height of the CA is in the range of 15 to 60 µm, following the tonotopic axis from distal to proximal (3). d, sensory dendrite; sc, scolopale cell. (*D–F*) Normalized magnitude of the DW (black lines) and the CC (blue lines) tonotopic response for different frequencies along the CA. Since a single reference was used for both structures (*Materials and Methods*), the graph conveys their relative vibration magnitude. In the axes labels, re ref means relative to the reference. (*G–I*) Normalized phase of the DW and the CC tonotopic response for different frequencies at the same stimulus frequencies as in *D–F*. DW wavelength estimates: 590, 455, and 346 µm, respectively. CC wavelength estimates: 370, 256, and 222 µm, respectively. These correspond to phase velocities of 3.7, 5.7, and 8.1 m/s (DW), respectively, and 2.4, 3.2, and 5.2 m/s (CC), respectively. (*J–L*) Mechanical tuning of the normalized magnitude of the DW and the CCs at different positions that are marked by their distance to the distal end of the CA. (*M–O*) Normalized phase of the DW and the CCs frequency tuning at the same positions as shown in *J–L*. DW group delay estimates: 344, 294, and 330 µs, respectively. CC group delay estimates: 454, 578, and 578 µs, respectively. (Data are from experiment BC0007, recorded through the intact cuticle. Stimulus level is 75 dB SPL.) Population data are in *SI Appendix*, Fig. S2. a, anterior; p, posterior; do, dorsal; di, distal.

Distinct Modes of Vibration within the CA. When comparing the tonotopic response with three distinct stimulus frequencies, the DW has a wider peak than the CC, and this widening is unilateral. Specifically, it is the proximal flank that is different between DW and CC (Fig. 3 *D–F*). The phase data (Fig. 3 *G–I*) reveal that the DW accumulates less phase between the distal end and the peak region. The frequency tuning of three different positions along the CA length (Fig. 3 *J–L*) shows that the DW is less sharply tuned. When recorded at the same distance from the distal end, the DW is tuned to higher frequencies than the CC. Finally, the DW phase curves are shallower than their CC counterparts, implying that DW vibrations have a shorter group delay than CC vibrations. These systematic differences between CC and DW vibration were observed in all animals tested (*SI Appendix*, Fig. S2). In the curves of Fig. 3 *M–O*, group delay for the CC exceeded that for the DW by 110, 284, and 248 µs, respectively. Since group delay is a metric of the latency with which the vibration energy arrives at the recording site (28), this suggests that the acoustic energy reaches the DW prior to reaching the CC.

Two Parallel but Shifted Place-Frequency Maps for the DW and the CC. Are the tuning differences between the two structures apparent on the whole length of the sensory tissue? To test for that, we measured vibrations on the DW and the CC along 800 µm of the CA using 33-µm steps, while presenting stimulus frequencies from 0.4 to 50 kHz in ∼950-Hz steps. The spatial and frequency sampling of our measurements allowed us to construct heat maps of the tuning of the two structures (Fig. 4 *A–D*). This way of presenting magnitude (Fig. 4 *A* and *B*) and phase data (Fig. 4 *C* and *D*) combines the spatial and spectral tuning shown separately in Fig. 3 *D–O*. We were able to determine the location of the spatial peak and the spatial 5-dB down points for each stimulus frequency, as indicated in the graphs. Consistent with the individual spectral and spatial tuning data in Fig. 3, the DW had a wider peak width than the CC over the entire frequency range, and the DW peaked more proximal than the CC peak. The phase responses confirm the greater accumulation of phase in the CC compared with the DW.

A detailed quantitative analysis of the tuning differences between CC and DW reveals that the tuning of the DW is shifted proximally compared with the CC (Fig. 4 *E* and *F*). The tuning of the DW is wider than that of the CC (Fig. 4*G*). The systematic differences between the tuning of the CC and the DW span the entire length of the hearing organ, as well as the entire spectral range tested (2.4 to 50 kHz). When averaged over this range, the

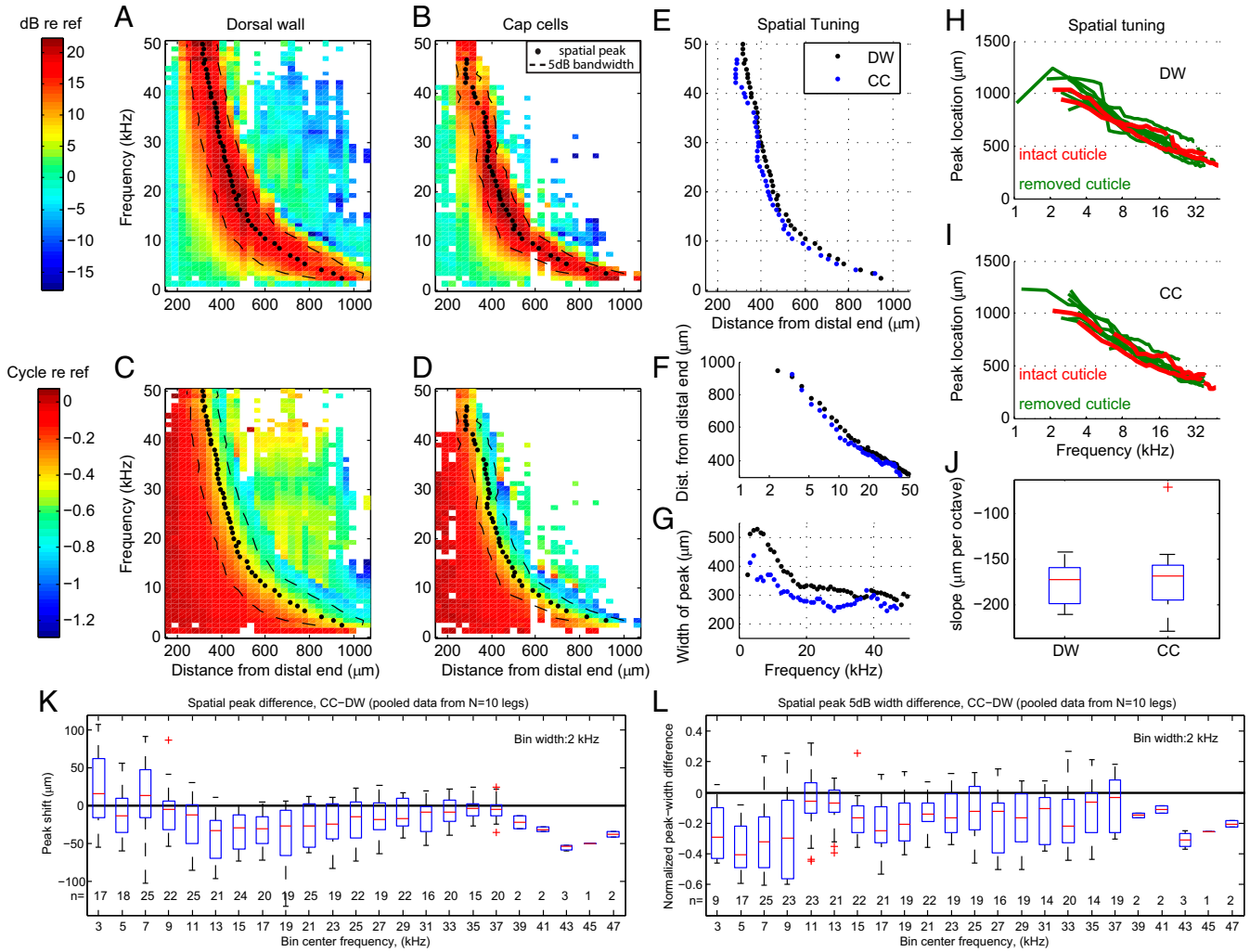

Fig. 4. Longitudinal vibration maps reveal tuning differences between the DW and the CC. (*A* and *B*) Normalized magnitude responses of (*A*) the DW and (*B*) the CC across different frequencies and recorded positions along the CA. The spatial peak for each frequency (black dot) and the associated 5-dB bandwidth (black lines) are overlaid. (*C* and *D*) Normalized phase responses of (*C*) the DW and (*D*) the CC across different frequencies and recorded positions along the CA. The spatial peak for each frequency (black dot) and the associated 5-dB bandwidth (black lines) are overlaid. (*E*) The frequency-dependent spatial peak per stimulus frequency for the DW and the CC. (*F*) The frequency-dependent spatial peak per stimulus frequency for the DW and the CC. In the log-lin axis, both tonotopic maps are approximately straight and parallel but shifted relative to one another. (*G*) The −5-dB peak width vs. stimulus frequency for the DW and the CC. (Data in *A*–*G* come from experiment BC0007. Stimulus level is 75 dB SPL. More data are in *SI Appendix*, Fig. S3.) (*H*) The place-frequency map of the DW across $n = 10$ hearing organs. (*I*) The place-frequency map of the CC across $n = 10$ hearing organs. (*J*) Median slopes of the 10 place-frequency maps are not significantly different. Data are extracted from *H* and *I*. (*K*) Population data of the relative peak position of CC vs. DW with $N = 10$ legs. Spatial peak locations were pairwise subtracted between DW and CC for each frequency. The difference was statistically evaluated using 2-kHz-wide bins. The boxes have lines at the lower quartile, the median, and the upper quartile values. Whisker pairs at each box show the extent of the rest of the data, with outliers marked by red plus signs. Individual bin sizes *n* are indicated. Over most of the frequency range, spatial peaks in the CC were shifted distally compared with the DW. (*L*) Corresponding comparison of the spatial peak width between DW and CC; the same $N = 10$ hearing organs as in *K*. Denoting the 5-dB down peak widths of the DW and the CC by W_{DW} and W_{CC}, respectively, their normalized difference is $\Delta = (W_{CC} - W_{DW})/W_{DW}$. Statistical analysis and layout are the same as in *K*. The spatial peaks in the CC were systematically narrower than the peaks in the DW. re ref, relative to the reference.

tuning difference amounts to 0.19 octaves in spectral terms (Fig. 4*E*) and 31 µm in spatial terms (Fig. 4*F*).

The current dataset allows for population metrics of the tuning of the two structures. The place-frequency maps of the DW and the CC of 10 hearing organs are shown in Fig. 4 *H* and *I*, respectively. Place-frequency maps of the DW and the CC motion from 10 different CAs show overlapping results, which imply that the used method of anchoring the different measurement positions to the distal end of the CA is robust. The DW and the CC share a similar slope on their place-frequency maps. Each octave of "best frequency" occupies 170 µm along the CA for both the DW and the CC (Fig. 4*J*), a stretch containing approximately nine sensory cells. The systematic differences in tuning between DW and CC were observed in all 10 animals tested, both in terms of peak location (Fig. 4*K*) and peak width (Fig. 4*L*).

Internal Motion within the CA. The relative motion of the DW and the CC is a candidate for the "drive" of transduction, as the two structures coincide with the two ends of the sensory dendrite, which is oriented perpendicular to the DW (Fig. 3*C* and *SI Appendix*, Fig. S5). The motion here is measured along the dorsal–ventral axis that is approximately parallel to that of the dendrite tip. The CC/DW magnitude ratio (Fig. 5*A*) shows that

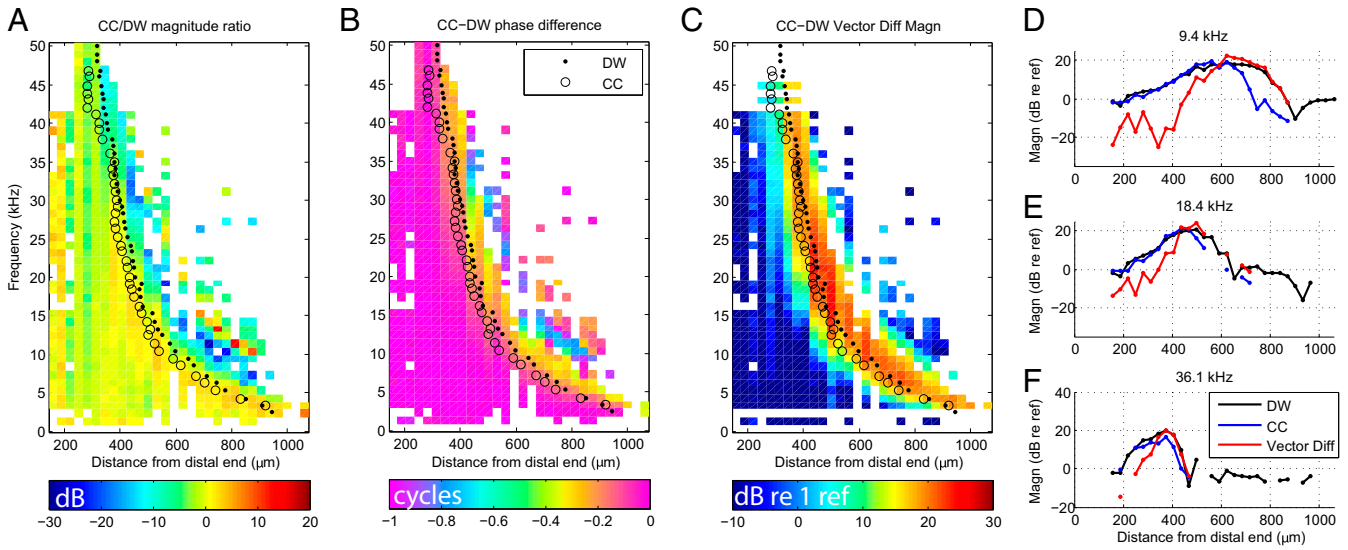

Fig. 5. Relative motion of CCs and the DW. (*A*) Color-coded magnitude difference (in decibels) between the CC and the DW mechanical response. Markers (point = DW, circle = CC) illustrate the spatial peak for each stimulus frequency, as in Fig. 4*E*. (*B*) Phase difference between the CC and the DW mechanical response of the same data as shown in *A*. (*C*) Magnitude of the vector difference between the DW and the CC mechanical response for the same data as displayed in *A* and *B*. (*D–F*) The tonotopic response of the DW, the CC, and their vector difference shown for three stimulus frequencies as indicated (data in *A–F* come from experiment BC0007). Stimulus level is 75 dB SPL. More data are in *SI Appendix*, Fig. S2. re ref, relative to the reference.

the two structures share similar magnitude of vibrations in positions distal to the spatial peak for each frequency. Proximal to the spatial peak, the DW magnitude dominates, resulting in negative dB values for the ratio. This analysis further characterizes how the CC magnitude decreases more distally than the DW magnitude (compare with Fig. 4).

The direct comparison of the phase between CC and DW (Fig. 5*B*) reveals that the two structures move in phase at positions distal to the spatial peak. Consistent with the examples in Fig. 3, the phase difference increases drastically at locations proximal to the spatial peak of each frequency. For most frequencies, the DW accumulates a phase lead over the CC of ∼0.25 cycles over a distance of just 30 to 70 μm proximal to the spatial peak, but for some frequencies, the difference is larger (up to ∼0.5 cycles). The location where the phase difference occurs coincides with the divergence of the amplitudes, again consistent with the three frequency examples shown in Fig. 3 *D–I*.

We further assessed the relative motion of CC and DW by computing the vector difference of their mechanical motions (i.e., taking into account both their relative amplitude and phase) (Fig. 5*C*). The spatial tuning of the vector difference was somewhat sharper than that of either structure (e.g., the 5-dB down peak widths in Fig. 5*D* were 286, 202, and 187 μm for the DW, CC, and vector differences, respectively). Toward the distal end, its magnitude was smaller than either individual motion. This is further illustrated in Fig. 5 *D–F*, which shows the tonotopic response of the DW, the CC, and their relative motion at three different stimulus frequencies: 9.4, 18.4, and 30 kHz. The differences are asymmetric; it is primarily the distal flank of the tonotopic response that is steeper for the vector difference data than it is for the DW and the CC.

The spectral data (magnitude vs. frequency) reveal a consistent asymmetric sharpening of the tuning of the vector difference data compared with the DW and the CC. It is primarily the steeper low-frequency flank that distinguishes the vector difference data from the data of DW and CC alone. The spectral tuning of the vector difference is shown for a total of nine experiments in *SI Appendix*, Fig. S2; a further example is shown in Fig. 6*E*.

Discussion

In summary, we recorded sound-induced vibrations in the bushcricket hearing organ using OCT vibrometry. The depth resolution of this technique yielded an unprecedented set of measurements. First, we measured the sound-induced motion of the anterior tympanum and the posterior tympanum at the same time. Our measurements confirmed that the two tympana bulged in and out simultaneously (27, 29) (Fig. 2*E*). Second, the septum between them followed the motion of the posterior tympanum (Fig. 2*B*). Third, we made a detailed and quantitative comparison between the sound-induced vibrations of the DW and the CC. The responses of both structures were tuned (Fig. 3), and there exist systematic differences between them in their tuning across the whole length of the sensory organ (Fig. 4). The differential motion of these structures was more sharply tuned than the absolute motion of either of them (Fig. 5 and *SI Appendix*, Fig. S2).

The tympana of the bushcricket hearing organ have been studied extensively, but their contribution to the hearing function is not entirely clear. Previous studies (17, 27) reported that the anterior and posterior tympana in different Tettigoniidae species moved inward and outward synchronously in response to sound. With LDV, one cannot measure the tympana simultaneously, and rearranging the preparation across recordings may have affected the microacoustic environment in these studies. Our simultaneous recordings provide a direct test of the relative motion of the tympani. Our data confirm and extend findings of previous studies (17, 27). Not only the two tympana, but also the adjacent septum bulge in and out simultaneously. This antiphasic motion may periodically stretch and squeeze the DW and the dorsally placed sensory epithelium. The dorsal part of the tympanum sits on top of incompressible hemolymph, so acoustic stimulation may cause a translocation of the CA. Such a coupling somewhat resembles the scheme proposed by ref. 17 in which the dorsal part of the tympana compresses the hemolymph overlying the CC, but the latter scheme depends on a tympanal plate mechanism in ref. 17 that we did not find in *M. elongata*. The resemblance of the two schemes is that CA motion is not directly driven by the air pressure in the trachea but indirectly,

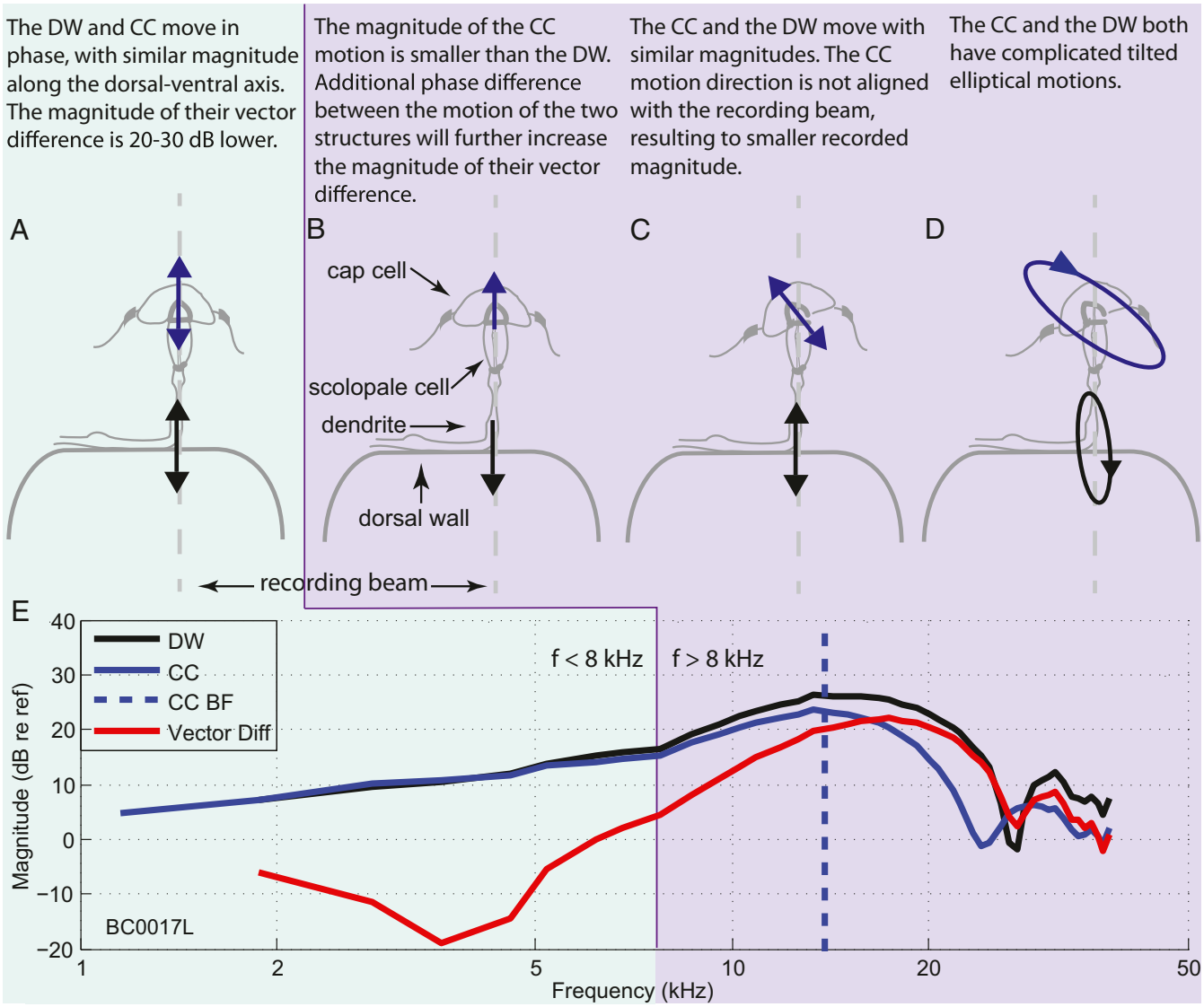

Fig. 6. Different geometric interpretations of the relative motion between DW and CC observed in this study. (*A*) In the absence of relative motion (here, <8 kHz; light green background), the DW and the CC move in phase and with similar magnitude along the dorsal–ventral axis (aligned with our recording beam). (*B–D*) Potential internal motion patterns that may underlie the observed differences in magnitude and phase (here, >8 kHz; light purple background). (*E*) Tuning curves of DW, CC, and their vector difference recorded at the medial part of the CA (experiment BC0017L, 79 dB SPL; BF, best frequency). Population data are from *SI Appendix*, Fig. S2.

either by the anterior tympanum and the septum through its connection to the posterior tympanum (Fig. 2) or via the tympanal plate and the hemolymph (17). The antiphasic motion of the tympana is likely to cause (or reflect) air pressure variations in the trachea, which will push and pull the adjacent DW, but the air–hemolymph interface may render this direct route inefficient. Intriguingly, the double-hinged motion (Fig. 2) shows a striking resemblance with the coupling of sound into vertebrate inner ears, where a lever system (middle ear ossicles) converts the larger motion of a larger surface (eardrum) to smaller motions of a smaller area (stapes). In vertebrate ears, this configuration provides an impedance match between airborne sound and the vibrations in the fluid-filled inner ear. The hinged motion of the bushcricket tympana and adjacent septum may well serve the same purpose.

Bangert et al. (27) reported that blocking the trachea spiracle with Vaseline decoupled the two tympana. Repeating these experiments while using OCT will allow the simultaneous measurement of the two tympana, the tracheal septum, and the CA. This may help to further disentangle the contribution of different acoustics paths to the bushcricket hearing organ. Phase differences along the ventral–dorsal axis of the tympanum, as shown in other bushcricket species (17), were not present in *M. elongata*.

The mechanotransduction channels in the CA sensory neurons are probably located at the tips of their cilia (11, 12), and they are commonly assumed to open and close upon longitudinal stretching of the sensory dendrite's cilium (30). Hummel et al. (12) in 2016 observed additional microtubules at the level of the scolopidial cap. They surrounded the ciliary tip and could therefore anchor filaments relevant to gating (31). In that case, transduction is likely to be driven by any relative motion between the DW and the CC since this would stretch and shorten the dendrite. Fig. 6 illustrates several potential realizations of this relative motion. A relative motion between the two structures along the dorsal–ventral axis would elongate and shorten the dendrite (Fig. 6*B*).

An anterior–posterior motion of the CC could also drive transduction, by pivoting of the sensory dendrite (Fig. 6*C*). Finally, a more complex elliptical motion of the two structures is possible, which could result in a frequency-dependent stretching and pivoting of the sensory dendrite (Fig. 6*D*). As will be discussed further in the following paragraphs, more measurement angles are needed to disentangle the different components of motion and thus, find the correct interpretation of the internal motion.

Our simultaneous recordings of the DW and the CC are a first step toward answering these questions. The systematic differences in tuning between the DW and the CC (Figs. 3 and 5 and *SI Appendix*, Fig. S2) indeed reveal a nontrivial relative motion between different structures within the CA. Stated differently, acoustic stimuli evoke a periodic deformation of the CA. Importantly, this micromechanical motion is sharply tuned. If transduction is indeed driven by such micromechanical motion, our data may explain discrepancies in best frequency and tuning sharpness between mechanical and neural tuning in the bushcricket CA (12). In particular, it would explain the sharper tuning of the neural response compared with the mechanics. A promising way to address such questions in future studies is to combine OCT vibrometry with neural recordings in the same hearing organ.

Our observations have implications for the understanding of the physical principles shaping the CA vibrations. Despite their close vicinity (15 to 60 μm apart, depending on longitudinal position), the DW and the CC differ in response phase, best frequency, and bandwidth. This calls for an explanation in terms of vibration mechanics. It is possible that the longitudinal stiffness and size gradients of the DW provide a preliminary stage of frequency selectivity, which is then further sharpened by local resonances of the individual scolopedia. The larger group delay of the CC compared with the DW (Fig. 3) is consistent with such a two-stage filtering. The hypothetical scheme is also reminiscent of the mammalian cochlea, where a physiologically robust, weakly tuned response is complemented by a physiologically vulnerable, sharply tuned response (18). Further exploration of such hypotheses will require a more detailed characterization of the micromechanical motion of the CA using OCT, combined with mathematical or numerical modeling.

The mapping of a wide audio range onto a short (<1-mm) sensory organ necessarily leads to a very dense representation of frequencies. The slope of the frequency-place map amounted to ∼170 μm per octave and was nearly identical in DW and CC (Fig. 4*J*). In comparison, the length of the unrolled cochlea is 35 mm in humans and 11 mm in gerbils, and the tonotopic slope in these species is 5,000 (32) and 1,500 μm per octave (33), respectively. Despite these large quantitative differences, it is remarkable that the tonotopic map is well represented by a straight line on a log-frequency scale in both the bushcricket (Fig. 4 *H* and *I*) and most mammals [with deviations occurring only at very low frequencies <500 Hz (34) and in some echolocating species that have an acoustic fovea (35)]. This striking similarity suggests that, despite vast anatomical differences (e.g., the basilar membrane is an interface between two fluids, whereas the DW is an interface between air and fluid) (*SI Appendix*, Fig. S5), common mechanisms may underlie frequency selectivity in the hearing organs of insects and mammals. Since these mechanisms are equally poorly understood in mammals and insects, any progress in the field of insect hearing may advance our understanding of mammalian hearing and vice versa. Species with well-accessible hearing organs like the bushcricket are highly suited for such comparative studies.

In mammals, the tonotopic map directly determines the density of neural representation of frequency bands because the spacing of sensory cells is uniform over the cochlear length. Thus, a typical (nonfoveal) mammalian map reveals an equal number of neural frequency channels per octave over most of the range, with a somewhat poorer representation toward the very lowest frequencies. In *M. elongata*, the lower frequencies are also less densely represented but this time because of the wider spacing of proximal sensory units (3). It is unclear whether this similarity is rooted in a common functional requirement.

In the context of comparative hearing science, it is also noteworthy that the spatial phase patterns in bushcrickets (e.g., Fig. 3) have their main features in common with those in the mammalian cochlea: an initial flat portion ending in a sharp downward kink followed by a steep downward slope ending in a plateau (36). Phase accumulation has been interpreted in terms of traveling waves in both mammals (32) and bushcrickets (19). The amount of phase lag accumulated at the peak location is larger in mammals (∼1.5 cycles) (18) than in the bushcricket (∼0.5 cycles), and this may reflect sharper tuning in the mammals (37). With all the similarities, one marked difference between the bushcricket and mammalian cochlea is the effect of sound intensity. Cochlear responses are very nonlinear; they show strongly compressive growth over a large dynamic range [68 dB of compression over a 96-dB range (18)]. Changes in sound intensity strongly and systematically affect sharpness of cochlear tuning and peak location of the wave (18) as well as its wavelength, phase velocity, and group velocity (28, 36). In comparison, the bushcricket CA is much more linear, only showing a slight compression (7 dB of compression over an 80-dB range, mostly concentrated at intensities >100 dB SPL), and there is no apparent effect of intensity on sharpness of tuning or wave propagation (16).

Although OCT vibrometry is a powerful technique for the study of hearing organs, it is important to briefly consider some limitations and potential ways to overcome them. Recorded vibrations are projections of the actual motion onto the recording beam. The more aligned the two are, the closer the measured magnitude resembles the actual magnitude. For our DW and CC recordings, we aligned the recording beam with the dorsal–ventral axis, which is perpendicular to the anterior–posterior alignment used for our tympanum recordings. A direct comparison between tympanum and CA motion magnitude is thus of limited scope. Our alignment choices optimize consistency with existing literature, but it is well possible that there exist other functionally relevant directions of motion between the DW and the CC that we failed to measure (Fig. 6). For a discussion of the spatial and directional interpretation of OCT vibrometry, we refer to ref. 25.

These geometric unknowns caution against oversimplification. It may appear attractive to interpret the different spatial phase profiles in CC and DW in terms of two "parallel waves" traveling at different speeds, but they may as well reflect a gradual change in vibration mode of a single wave (38). A more comprehensive exploration of the micromechanics of the bushcricket CA will require measuring the same structures from different angles, so that different directions of motion can be disentangled. In the current study, we did image the CA from both an anterior–posterior view and a dorsal–ventral view. At this stage, however, we cannot determine the direction of motion with certainty. This would require a reliable method of registration, ensuring that the exact same location is targeted across viewing angles. In the literature, the lateralization of the CC responses toward the anterior side of the CA has been described (39). With a validated registration method, one could record the CC from the two angles mentioned above, test whether the CC indeed pivots around the scolopale cell, and assess the relevance of this motion for tuning.

Other complications may arise from uncertainties in interpreting OCT images in heterogeneous tissues. Our study demonstrates that OCT produces anatomically faithful images of the bushcricket hearing organ (Figs. 1 *B–D*, 2 *A–C*, and 3*B*). The

same technique has been used to study the morphogenesis of insects in a noninvasive manner (40) and insect heart pulsations (41). OCT imaging is based on the delay times of backscattered light from different depths of the sample, which not only depend on the path length but also, on the speed of light of the medium as quantified by its refractive index n. For a homogeneous medium, the delay times are easily corrected for the refractive index. The insect leg, however, is heterogeneous; it is partly filled with fluid (hemolymph, $n \approx 1.5$) and partly with air ($n \approx 1$). Fig. 2 illustrates this; the dorsal, hemolymph-filled part of the leg is distorted compared with the ventral, air-filled part. Detailed knowledge of the refractive index of the imaged structures would enable one to correct for such imaging artifacts, but the optical characterization of the bushcricket hearing organ exceeded the purposes of the current study.

This study has employed the opportunities for studying nonvertebrate hearing organs offered by OCT vibrometry. It revealed complexities in the micromechanics of the bushcricket CA that had not been found with previous methods. On the one hand, these findings bring new challenges in understanding insect hearing. On the other, they offer new views and suggest new solutions to known fundamental problems, including the delivery path of acoustic energy to the sensory tissue, the biophysics of auditory frequency selectivity, and the exact mechanisms that drive transduction. From a wider perspective, current technology facilitates the comparative study of hearing organs in general and the similarities and differences between hearing in insects and mammals in particular. For all these scientific problems, we now have the technical means to explore them. This opens up a wide range of theoretical and experimental exploration of hearing in miniaturized systems, with numerous technical and scientific applications.

Materials and Methods

Animal Preparation. In total, 19 bushcrickets of the species *M. elongata* were used for in vivo sound-induced vibration measurements on the CA and the tympana. CA recordings were made on 11 individual tibial hearing organs belonging to nine animals. The animals were anesthetized by lowering their body temperature after placing them in a container filled with ice. When they were not responsive (usually after ~10 min) and their mandibles were loose, their middle and rear legs were removed. The animal was placed with its thorax on the animal holder, and it was stabilized using melted medical wax. The front legs were stabilized in a position where the CAs were accessible to the OCT beam. In two particular experiments (BC0007, BC00013), it was possible to record through the intact cuticle. The individual measurements that are shown in the current report come from experiment BC0007. For other animals, the dorsal cuticle obscured the view of the CA. For that reason, it was removed surgically and replaced by a glass coverslip. After the cuticle removal, the CAs were inspected using OCT imaging to ensure they were not harmed by the preparation. Viewing through the glass coverslip allowed us to identify the underlying structures and perform mechanical measurements, and it is a common method in mammal hearing research (42). As was the case in previous bushcricket studies (19), there are no signs that removing the cuticle adversely affected auditory sensitivity. The population data in are combined from animals with an intact cuticle and animals with the cuticle removed. Tympanum measurements were obtained by placing the anterior tympanum perpendicular to the OCT beam. All measurements were acquired in vivo. In total, tympanum measurements were acquired from 11 legs belonging to different animals. At the end of the experiment, the animal was anesthetized and subsequently killed by decapitation.

Acoustic Stimulation. Broadband multitone "zwuis" complexes (43) were used, following an open-field stimulation paradigm, using a ScanSpeaker R2904/700 005 loudspeaker placed 35 cm from the animal inside a soundproof booth. The ipsilateral acoustic trachea opening on the thorax was facing the loudspeaker. Calibration of the sound pressure was done by temporarily replacing the animal holder by a microphone. The surfaces of the OCT probe, animal holder, etc., were covered with cotton wool in order to minimize acoustic reflections. The most commonly used broadband stimulus consisted of 51 spectral components, spanning from 0.4 to 50 kHz (average frequency spacing: 990 Hz), presented at 75, 79, or 85 dB per component. All the spectral components had equal amplitudes, with levels expressed in decibels re 20 μPa (i.e., decibels SPL), but the stimulus phase was randomized across frequency. Each stimulus was presented for 12 s, and interstimulus intervals lasted for ~60 s.

OCT Imaging and Vibrometry. Vibration measurements were obtained using OCT. More details on the experimental setup are in ref. 25. OCT is an imaging technique, based on low-coherence interferometry. A spectral domain - optical coherence tomography system (Thorlabs Telesto TEL320C1) was used for interferometric imaging and vibration measurements. Its field of view is 10 × 10 mm; its depth range is 3.5 mm. The working distance of the objective was 24 mm. Cross-sectional (B scan) and axial images (A and M scans) were triggered externally using monophasic rectangular pulses phase locked to the acoustic stimulation system (Tucker Davies Technologies System III) at a sampling rate of 111.6 kHz. The optics of our recording system (Mitotoyu IR imaging lens with a numerical aperture of 0.055) introduced an axial point spread function of 6-μm full width half maximum and a lateral resolution (in the *xy* plane) of 13 μm (all assessed in air, with a refractive index of one). For our dorsal view measurements, the OCT measurement beam was manually aligned with the dorsal–ventral anatomical axis of the CA. The vibration measurements that we made should therefore be favoring measuring vibrations along this axis.

The refractive index n of the various anatomical structures affects the recorded vibration magnitude. Phase data are not affected by n, whereas magnitude is shifted upward by $20 \log n \approx 3$ dB for most fluids. The effect of correcting the data for n is illustrated in *SI Appendix*, Fig. S4, including the case where DW and CC have different n, motivated by the suggestion that fluid composition between the CC and the DW may differ from that of the hemolymph canal around the CA (14, 17). Since the corrections are small and uniform and the proper n values are unknown, we did not apply such corrections to the figures.

The anatomy of the distal end of the CA is quite distinct, and it is possible to define the same anatomical structure across experiments. In order to compare recorded positions across animals, we therefore used the distal end of the hearing organ as an anchor point. The recorded structures were labeled by the horizontal distance between the measuring beam and the vertical line that intersects the distal end of the CA (the red line in Fig. 1*C*). The depth resolution of the OCT allowed us to record the DW and the CC simultaneously, along one recording beam, at different positions of the CA. That way, a DW measurement and a CC measurement obtained from the same beam shared the same distance from the distal end of the CA.

Response Analysis. Mechanical vibrations were obtained from 1) the DW and the CCs and 2) both tympana and septum. Responses were analyzed by Fourier transformation of the vibration waveforms derived from contiguous groups of three pixels in each M scan, where each pixel covers a depth of 3 μm, depending on the exact value of the refractive index of the structures. Each frequency component in a vibration measurement was assessed using the Rayleigh test ($p = 0.001$) for significance of phase locking (44). Upon repeated recordings, vibration magnitude and phase are typically reproduced to within 0.5 dB and 0.02 cycle, respectively. The mechanical measurements from the CA were normalized to vibrations recorded on the distal end of the organ (green marker in Fig. 1*C*) analogous to normalization using the middle ear ossicles commonly used in the field of cochlear mechanics (45). This accounted for imperfection in the calibration of the acoustics. We made sure that the reference vibration measurement and the CA recordings were performed while using the exact same configuration, in particular the same height of the adjustable optical probe. The use of a mechanical reference rather than a microphone makes the data less suited for the estimation of acoustic transfer functions, but it is adequate for the aims of the present study, namely the direct comparison of vibrations across different locations in a single hearing organ. The absence of ripples in normalized magnitude–frequency data (e.g., Fig. 3 *D–F*) indicates that any acoustic reflections had little impact on our recordings.

Different recorded positions are identified by their distance from the most distal part of the CA, as shown with a red vertical line in Fig. 1*C*. Data were analyzed using custom software developed in the MatLab (MathWorks, USA) environment. The spatial and spectral peaks were detected by using a polynomial fit on a 15-dB range around the peak of the normalized magnitude data. The order of the polynomial varied from second to fourth,

according to the number of fitting points that fulfilled the 15-dB-range criterion. In a minority of cases, manual exclusion of the fitting points was applied if the automated peak detection algorithm failed. Phase averaging (indicated as white stripes in Fig. 2*B*) was obtained as follows. The phases ϕ_k of individual pixels in each subdomain (anterior and posterior tympanum) were determined by taking the angle of $\sum_k \exp(i\phi_k)$, where i is the square root of -1.

Group delay was estimated from the data in Fig. 3 *M–O* by fitting straight lines to the portions of the phase-frequency curves that correspond to the magnitude peaks (highest 10 dB) in Fig. 3 *J–L*. The reported group delay estimates are the negative slopes of these fit lines. Wavelengths and phase velocity were derived from the data in by fitting straight lines to the portions of the phase-position curves that correspond to the magnitude peaks (highest 10 dB) in Fig. 3 *D–F*. Wave number estimates (k in cycles per micrometer) are the negative slopes of these fit lines. Wavelength λ and phase velocity c were derived from k by $\lambda = 1/k$ and $c = f/k$, respectively, with f the stimulus frequency.

Data Availability. Vibration measurement data have been deposited in Figshare (https://figshare.com/authors/Marcel_van_der_Heijden/5457377). Data for the figures have been deposited in Figshare (https://figshare.com/articles/dataset/Vavakou_Scherberich_Nowotny_vanderHeijden_2021/15292230). All other study data are included in the article and/or *SI Appendix*.

ACKNOWLEDGMENTS. We thank Ana-Maria Marchidan for help with the illustrations. This work was supported by Deutsche Forschungsgemeinschaft Grant 841/8-1.

1. J. Hummel, K. Wolf, M. Kössl, M. Nowotny, Processing of simple and complex acoustic signals in a tonotopically organized ear. *Proc. Biol. Sci.* **281**, 20141872 (2014).
2. J. Strauß, G. U. C. Lehmann, A. W. Lehmann, R. Lakes-Harlan, Spatial organization of tettigoniid auditory receptors: Insights from neuronal tracing. *J. Morphol.* **273**, 1280–1290 (2012).
3. J. Hummel, M. Kössl, M. Nowotny, Morphological basis for a tonotopic design of an insect ear. *J. Comp. Neurol.* **525**, 2443–2455 (2017).
4. D. B. Lewis, The physiology of the tettigoniid ear. II. The response characteristics of the ear to differential inputs: Lesion and blocking experiments. *J. Exp. Biol.* **60**, 839–851 (1974).
5. E. Hoffmann, M. Jatho, The acoustic trachea of tettigoniids as an exponential horn: Theoretical calculations and bioacoustical measurements. *J. Acoust. Soc. Am.* **98**, 1845–1851 (1995).
6. A. Michelsen, K. G. Heller, A. Stumpner, K. Rohrseitz, A new biophysical method to determine the gain of the acoustic trachea in bushcrickets. *J. Comp. Physiol. A Neuroethol. Sens. Neural Behav. Physiol.* **175**, 145–151 (1994).
7. D. Veitch *et al*., A narrow ear canal reduces sound velocity to create additional acoustic inputs in a microscale insect ear. *Proc. Natl. Acad. Sci. U.S.A.* **118**, e2017281118 (2021).
8. R. Heinrich, M. Jatho, K. Kalmring, Acoustic transmission characteristics of the tympanal tracheae of bushcrickets (tettigoniidae). II. Comparative studies of the tracheae of seven species. *J. Acoust. Soc. Am.* **93**, 3481–3489 (1993).
9. J. Hummel, M. Kössl, M. Nowotny, Sound-induced tympanal membrane motion in bushcrickets and its relationship to sensory output. *J. Exp. Biol.* **214**, 3596–3604 (2011).
10. R. Schumacher, Scanning-electron-microscope description of the tibial tympanal organ of the tettigonioidea (Orthoptera, Ensifera). *Z. Morphol. Tiere* **81**, 209–219 (1975).
11. J. E. Yack, The structure and function of auditory chordotonal organs in insects. *Microsc. Res. Tech.* **63**, 315–337 (2004).
12. J. Hummel *et al*., Gating of acoustic transducer channels is shaped by biomechanical filter processes. *J. Neurosci.* **36**, 2377–2382 (2016).
13. B. P. Oldfield, Tonotopic organisation of auditory receptors in tettigoniidae (Orthoptera: Ensifera). *J. Comp. Physiol.* **147**, 461–469 (1982).
14. F. Montealegre-Z, D. Robert, Biomechanics of hearing in katydids. *J. Comp. Physiol. A Neuroethol. Sens. Neural Behav. Physiol.* **201**, 5–18 (2015).
15. Y. Lin, K. Kalmring, M. Jatho, T. Sickmann, W. Rössler, Auditory receptor organs in the forelegs of *Gampsocleis gratiosa* (tettigoniidae): Morphology and function of the organs in comparison to the frequency parameters of the conspecific song. *J. Exp. Zool.* **267**, 377–388 (1993).
16. A. Palghat Udayashankar, M. Kössl, M. Nowotny, Tonotopically arranged traveling waves in the miniature hearing organ of bushcrickets. *PLoS One* **7**, e31008 (2012).
17. F. Montealegre-Z, T. Jonsson, K. A. Robson-Brown, M. Postles, D. Robert, Convergent evolution between insect and mammalian audition. *Science* **338**, 968–971 (2012).
18. L. Robles, M. A. Ruggero, Mechanics of the mammalian cochlea. *Physiol. Rev.* **81**, 1305–1352 (2001).
19. E. S. Olson, M. Nowotny, Experimental and theoretical explorations of traveling waves and tuning in the bushcricket ear. *Biophys. J.* **116**, 165–177 (2019).
20. A. Michelsen, O. N. Larsen, Biophysics of the ensiferan ear. *J. Comp. Physiol.* **123**, 193–203 (1978).
21. M. C. Göpfert, H. Briegel, D. Robert, Mosquito hearing: Sound-induced antennal vibrations in male and female Aedes aegypti. *J. Exp. Biol.* **202**, 2727–2738 (1999).
22. F. A. Sarria-S, B. D. Chivers, C. D. Soulsbury, F. Montealegre-Z, Non-invasive biophysical measurement of travelling waves in the insect inner ear. *R. Soc. Open Sci.* **4**, 170171 (2017).
23. S. S. Gao *et al*., In vivo vibrometry inside the apex of the mouse cochlea using spectral domain optical coherence tomography. *Biomed. Opt. Express* **4**, 230–240 (2013).
24. S. S. Gao *et al*., Vibration of the organ of Corti within the cochlear apex in mice. *J. Neurophysiol.* **112**, 1192–1204 (2014).
25. N. P. Cooper, A. Vavakou, M. van der Heijden, Vibration hotspots reveal longitudinal funneling of sound-evoked motion in the mammalian cochlea. *Nat. Commun.* **9**, 3054 (2018).
26. E. S. Olson, C. E. Strimbu, Cochlear mechanics: New insights from vibrometry and optical coherence tomography. *Curr. Opin. Physiol.* **18**, 56–62 (2020).
27. M. Bangert *et al*., Stimulus transmission in the auditory receptor organs of the foreleg of bushcrickets (Tettigoniidae) I. The role of the tympana. *Hear. Res.* **115**, 27–38 (1998).
28. M. van der Heijden, C. P. Versteegh, Energy flux in the cochlea: Evidence against power amplification of the traveling wave. *J. Assoc. Res. Otolaryngol.* **16**, 581–597 (2015).
29. T. Jonsson, F. Montealegre-Z, C. D. Soulsbury, K. A. Robson Brown, D. Robert, Auditory mechanics in a bush-cricket: Direct evidence of dual sound inputs in the pressure difference receiver. *J. R. Soc. Interface* **13**, 20160560 (2016).
30. A. S. French, Transduction mechanisms of mechanosensilla. *Annu. Rev. Entomol.* **33**, 39–58 (1988).
31. X. Liang *et al*., A NOMPC-dependent membrane-microtubule connector is a candidate for the gating spring in fly mechanoreceptors. *Curr. Biol.* **23**, 755–763 (2013).
32. G. Von Békésy, *Experiments in Hearing* (McGraw-Hill, 1960).
33. M. Müller, The cochlear place-frequency map of the adult and developing Mongolian gerbil. *Hear. Res.* **94**, 148–156 (1996).
34. D. D. Greenwood, Comparing octaves, frequency ranges, and cochlear-map curvature across species. *Hear. Res.* **94**, 157–162 (1996).
35. M. Kössl, M. Vater, "Cochlear structure and function in bats" in *Hearing by Bats*, A. N. Popper, R. R. FaySpringer Handbook of Auditory Research, vol. 5, Springer, New York, NY, 1995), pp. 191–234.
36. M. van der Heijden, N. P. Cooper, "Wave propagation in the mammalian cochlea" in *In to the Ear and Back Again: Advances in Auditory Biophysics, Proceedings of the 13th Mechanics of Hearing Workshop*, C. Bergevin, S. Puria, Eds. (AIP Publishing LLC, Melville, NY, 2018), vol. 1965, p. 080002.
37. P. X. Joris *et al*., Frequency selectivity in Old-World monkeys corroborates sharp cochlear tuning in humans. *Proc. Natl. Acad. Sci. U.S.A.* **108**, 17516–17520 (2011).
38. M. van der Heijden, Frequency selectivity without resonance in a fluid waveguide. *Proc. Natl. Acad. Sci. U.S.A.* **111**, 14548–14552 (2014).
39. A. Palghat Udayashankar, M. Kössl, M. Nowotny, Lateralization of travelling wave response in the hearing organ of bushcrickets. *PLoS One* **9**, e86090 (2014).
40. M. Nioi, P. E. Napoli, S. M. Mayerson, M. Fossarello, E. d'Aloja, Optical coherence tomography in forensic sciences: A review of the literature. *Forensic Sci. Med. Pathol.* **15**, 445–452 (2019).
41. M. A. Choma, S. D. Izatt, R. J. Wessells, R. Bodmer, J. A. Izatt, Images in cardiovascular medicine: In vivo imaging of the adult *Drosophila melanogaster* heart with real-time optical coherence tomography. *Circulation* **114**, e35–e36 (2006).
42. N. P. Cooper, W. S. Rhode, Nonlinear mechanics at the apex of the guinea-pig cochlea. *Hear. Res.* **82**, 225–243 (1995).
43. M. van der Heijden, P. X. Joris, Cochlear phase and amplitude retrieved from the auditory nerve at arbitrary frequencies. *J. Neurosci.* **23**, 9194–9198 (2003).
44. C. P. Versteegh, M. van der Heijden, Basilar membrane responses to tones and tone complexes: Nonlinear effects of stimulus intensity. *J. Assoc. Res. Otolaryngol.* **13**, 785–798 (2012).
45. W. S. Rhode, Observations of the vibration of the basilar membrane in squirrel monkeys using the Mössbauer technique. *J. Acoust. Soc. Am.* **49**, 1218 (1971).